J. Fluid Mech. (2020), *vol.* 891, A13. © The Author(s), 2020.
Published by Cambridge University Press
doi:10.1017/jfm.2020.145

Vortex moment map for unsteady incompressible viscous flows

Juan Li[1], Yinan Wang[1], Michael Graham[2] and Xiaowei Zhao[1,†]

[1]School of Engineering, The University of Warwick, Coventry CV4 7AL, UK

[2]Department of Aeronautics, Imperial College, London SW7 2BY, UK

(Received 29 October 2019; revised 19 January 2020; accepted 18 February 2020)

In this paper, a vortex moment map (VMM) method is proposed to predict the pitching moment on a body from the vorticity field. VMM is designed to identify the moment contribution of each given vortex in the flow field. Implementing this VMM approach in starting flows of a NACA0012 airfoil, it is found that, due to the rolling up of leading-edge vortices (LEVs) and trailing-edge vortices (TEVs), the unsteady nose-down moment about the quarter chord is higher than the steady-state value. The time variation of the unsteady moment is closely related to the LEVs and TEVs near the body and the VMM gives an intuitive understanding of how each part of the vorticity field contributes to the pitching moment on the body.

Key words: vortex shedding, separated flows

1. Introduction

An understanding of the dynamic variation of pitching moment is key to analysing a range of dynamic problems, including buffeting of long-span suspension bridges (Zhao *et al.* 2016), the phenomenon of stall flutter on helicopters (Ham & Maurice 1966) and wind turbines (Hansen 2007) as well as flapping flight (Krashanitsa *et al.* 2009), particularly when the wings or lifting sections are very flexible in torsion. In these cases, which involve either bluff bodies or leading-edge separation, the unsteady effect of the pitching moment can play a very important role in the stability and dynamic response of the body when coupled to the effects of structural compliance or rigid-body dynamics (Ham & Maurice 1966). Therefore, there is a very practical interest in calculating the unsteady pitching moment on a body, especially in separated flows.

Analytical methods are only possible in limited circumstance for some steady and unsteady flows, viscosity being ignored, and are not possible for separated flows. A detailed knowledge of the entire vorticity field is always required (Batchelor 1967). There has been more success with analytical–numerical coupling methods adopting unsteady thin airfoil theory corrected by additional vortices (Ramesh *et al.* 2014; Li & Wu 2015, 2016; Fernandez-Feria & Alaminos-Quesada 2018) or an unsteady Blasius equation (Xia & Mohseni 2017). Advances in experimental techniques have led to accurate measurements on fluid dynamic loads on lifting surfaces (Devoria, Carr &

† Email address for correspondence: Xiaowei.zhao@warwick.ac.uk

Ringuette 2014; Ramesh *et al.* 2014; Mancini *et al.* 2015). However, direct load measurements are complicated by a number of issues. At low Reynolds numbers, the fluid dynamic loads tend to be very small and are subject to significant measurement errors (DeVoria *et al.* 2014). Moreover, in unsteady cases the measurement can be significantly contaminated by resonance of the test piece with structural compliance in the force balance, due to the need to measure the strain induced by the small fluid loads. Meanwhile, the velocity field data from unsteady flow experiments are readily available due to the development of particle image velocimetry (PIV) as a non-intrusive flow field measurement technique. Attempts to circumvent the direct measurement of loads gave rise to force and moment methods from the velocity field, including a vortical impulse integration (Wu 1981; Graham, Pitt Ford & Babinsky 2017) and an auxiliary potential-based method (Howe 1995; Li & Wu 2018). But the typical method in computational fluid dynamics (CFD) to obtain fluid dynamic loads from an integration of computed surface pressures and skin friction is very difficult to apply to unsteady PIV data due to the difficulty of simultaneously resolving the entire boundary layer to a sufficient resolution near the solid surface (DeVoria *et al.* 2014).

Methods relating flow structures to fluid dynamic loads have seen many developments since the pioneering work of Polhamus (1966), who attributed the high lift production in a delta wing to the stabilized leading-edge vortex (LEV) by the axial flow effect. Qualitatively, the unsteady LEV has been shown to be primarily responsible for the large transient lift generation in flapping flight (Ellington *et al.* 1996; Pitt Ford & Babinsky 2013), whereas the roll-up of a trailing-edge vortex (TEV) has been shown to reduce the lift production (Dickinson & Gotz 1993). More recently, Eldredge & Jones (2019) and Chiereghin, Cleaver & Gursul (2019) explored the relevance between generation of unsteady forces and flow structures. Other works quantitatively derived formulae relating fluid dynamic forces to either the velocity field and its spatial/temporal derivatives (Lin & Rockwell 1996; Noca 1996; Noca, Shiels & Jeon 1997; Zhu, Bearman & Graham 2002; Wu, Lu & Zhuang 2007) or the velocity and vorticity fields (Howe 1995). Furthermore, vortex force maps (VFMs) were constructed (Li & Wu 2018) to identify the contributions of force from each given vortex in the flow field. However, the relationship between pitching moment and flow structures has not been as fully explored as the lift or drag forces.

This work derives the VMM method with the help of the hypothetical potential suggested by Howe (1995) as an extension of the VFM method. The VMMs, which ensure vortices far away from the body have negligible effect on the body moment, are built to identify the moment contribution of each given vortex. To demonstrate its applications, the proposed vortex moment method is used to study impulsively started flows around a NACA0012 airfoil, where the added mass effect is zero at all times except the initial moment. CFD is used here to provide the flow field data as input to the VMM method and provides moment results as validation of the proposed method. The time-averaged solutions of the moment obtained by CFD are compared with experimental results by Ohtake, Nakae & Motohashi (2007) and Rainbird (2016). The VMMs are used to provide a better understanding of the relationship between the unsteady moment oscillation and the vortical structure in the flow field.

In § 2, the derivation of the VMM approach is presented. Then, in § 3, we will demonstrate the analyses of VMM for a NACA0012 airfoil. Section 4 is devoted to the application of the VMM approach to unsteady starting flows around a NACA0012 airfoil at different Reynolds numbers and angles of attack (AoAs). The theoretical results of force variation with time are verified against CFD results. Lastly, concluding remarks are given in § 5.

2. Vortex moment expression for incompressible viscous flows

Consider two-dimensional unsteady viscous flows of constant density ρ and viscosity μ around a solid body (e.g. a general airfoil) of volume Ω_B, bounded by a closed curve l_B. The control volume Ω is bounded by l_∞ at infinity. In the body-fixed frame (x, y), the free-stream velocity is V_∞, incident at an angle α to the body axis. At any instant, the velocity field of the resulting flow is $\boldsymbol{U} = (u, v)$, and the vorticity $\omega_z = (\partial v/\partial x) - (\partial u/\partial y)$. In a previous work, the two-dimensional VFM method was derived for general airfoils (Li & Wu 2018). It was shown that the instantaneous force F_k on a two-dimensional body in the kth-direction can be expressed as

$$F_k = \rho \iint_\Omega \boldsymbol{\Lambda}_k \cdot \boldsymbol{U}\omega_z \,\mathrm{d}\Omega, \tag{2.1}$$

where the vortex force vector $\boldsymbol{\Lambda}_k = (\partial\phi_k/\partial y, -\partial\phi_k/\partial x)$ is a function of a hypothetical potential ϕ_k defined as the velocity potential induced by unit incident velocity of ideal flow in the kth-direction. The vortex force vector is normalized by the free-stream velocity according to its definition and it is a non-dimensional vector coefficient introduced here to calculate the aerodynamic force when the real flow velocity and vorticity are given. It is dependent only on the geometry of the body and not the flow field, which allows for the construction of a flow-independent VFM for a given body.

For the pitching moment M_p acting on the body at point $\boldsymbol{x}_p$, we can assume a similar form of expression

$$M_p = \rho\zeta \iint_\Omega \boldsymbol{F}_p \cdot \boldsymbol{U}\omega_z \,\mathrm{d}\Omega. \tag{2.2}$$

Here, ζ is the characteristic length of the body and the moment is counterclockwise positive (a positive value means a nose-down pitching moment for flow coming from the left). Obtaining the VMM vector $\boldsymbol{F}_p$ will allow a similar map to be constructed for the moment M_p on the body. Although there is no simple analogue between the vortex force vector $\boldsymbol{\Lambda}_k$ and the VMM vector $\boldsymbol{F}_p$, luckily, we can derive the expression for $\boldsymbol{F}_p$ from the integral moment theory of Howe (1995), where the moment of a rigid body due to free vortices in the body-fixed frame is

$$M_p = \rho \iint_\Omega \nabla\chi_p \cdot (\boldsymbol{\omega} \times \boldsymbol{U}) \,\mathrm{d}\Omega. \tag{2.3}$$

Here, the hypothetical potential χ_p is defined as the velocity potential for hypothetical fluid motion induced by the rotation of the body Ω_B at unit angular velocity about an axis that passes through the reference point $\boldsymbol{x}_p$ and is perpendicular to the coordinate plane. Since we consider the application of the starting flow problem, the added mass force is zero at any instant after the starting process. The skin friction is also neglected here since the CFD results in the next section show its contribution is very small, even at low Reynolds numbers. By comparing (2.3) with (2.2), the VMM vector $\boldsymbol{F}_p$ can be obtained as

$$\boldsymbol{F}_p = \frac{1}{\zeta}\left(\frac{\partial\chi_p}{\partial y}, -\frac{\partial\chi_p}{\partial x}\right). \tag{2.4}$$

The VMM vector $\boldsymbol{F}_p$ is normalized by a unit angular velocity multiplied by the characteristic length. It is independent of the flow field and only dependent on the

geometry of the body. According to the definition of hypothetical potential χ_p, it satisfies the following Laplace equation and boundary conditions:

$$\left.\begin{array}{c} \nabla^2\chi_p = 0, \\ \dfrac{\partial\chi_p}{\partial n} = \left(\boldsymbol{x} - \boldsymbol{x}_p\right) \times \boldsymbol{p} \cdot \boldsymbol{n} \quad (x, y) \to l_B, \\ \nabla\chi_p = 0 \quad (x, y) \to \infty, \end{array}\right\} \tag{2.5}$$

where $\boldsymbol{n}$ is the normal vector pointing inward from the body surface, and the unit vector along the moment axis is denoted as $\boldsymbol{p}$. The hypothetical potential χ_p vanishes at infinity and is made unique by requiring no circulation about any irreducible path. Thus, a closed-form expression for the VMM method around a body is obtained.

The VMM vector $\boldsymbol{F}_p$ facilitates the construction of a flow-independent VMM which can be used to analyse the moment contribution of each given vortex in the flow field, as will be shown in § 3. On the other hand, with the real flow velocity and vorticity identified from the velocity field either from the mesh grids on CFD or PIV, the pre-computed VMM vector can be used to calculate the total pitching moment acting on the body. An example of extracting pitching moment from CFD field will be given in § 4.

3. Vortex moment map analysis for a NACA0012 airfoil

In this section, a NACA0012 airfoil is used to demonstrate how VMMs are built and to identify the moment contribution effect of each given vortex according to its position, strength and local velocity.

For the NACA0012 airfoil with a chord length of c aligned with the x-axis ($x/c \in [0, 1]$), the reference points $\boldsymbol{x}_p = (x_p, 0)$ ($p = 1, 2, 3$ and 4) are chosen as the leading edge (LE, $x_1/c = 0$), the quarter chord ($x_2/c = 1/4$, which is the aerodynamic centre for a variety of airfoils including NACA0012 airfoil), the half-chord ($x_3/c = 1/2$) and the trailing edge (TE, $x_4/c = 1$), respectively. To obtain the hypothetical potential χ_p ($p = 1, 2, 3$ and 4), the Laplace equations (2.5) with four different p are solved numerically by using a vortex panel method as suggested by Katz & Plotkin (2001) in solving the steady-state potential flow. This vortex panel method solves the Laplace equation via a superposition of singularity elements on the body surface and enforces the non-penetration boundary condition on the surface. For rotating bodies, the requirement of no circulation about any irreducible path should also be imposed and a uniformly distributed vorticity with strength -2 must be deployed to describe the solid-body motion (Koumoutsakos, Leonard & Pepin 1994), so that the correct potential solution may be reached. The method has been validated against the analytical solution for a circular cylinder. The VMM vectors $\boldsymbol{F}_p$ ($p = 1, 2, 3$ and 4) are then computed by (2.4).

With the VMM vectors precomputed, the VMMs here are plotted in the two-dimensional plane (x, y) and contain vortex moment lines that are locally parallel to the VMM vector $\boldsymbol{F}_p$. Vortex moment lines, independent of specific flow conditions (including Reynolds number), can be obtained through a streamline procedure, with the velocity replaced by the vortex force factors. The moment contribution of any individual vortex can be identified according to its circulation (sign and magnitude), position and direction (the angle between the vortex force line and streamline at the position of the vortex). Meanwhile, the norm of the VMM vector $|\boldsymbol{F}_p|$ is also presented in the map as contour lines to analyse the magnitude of the effect on the moment.

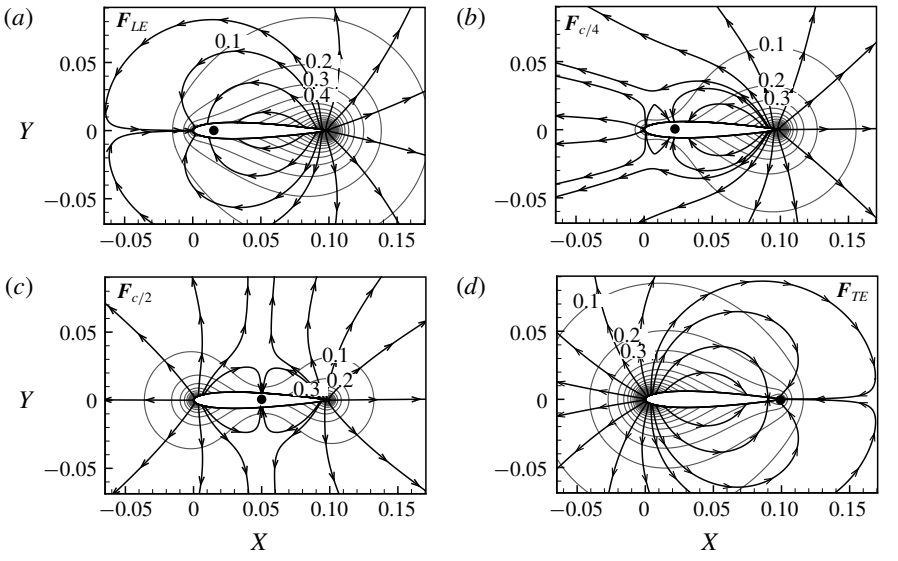

FIGURE 1. Vortex moment maps for NACA0012 airfoil with different reference points: (*a*) moment map about the LE; (*b*) moment map about $c/4$; (*c*) moment map about $c/2$; (*d*) moment map about the TE. The lines with arrows are vortex moment lines locally parallel to the vector $\boldsymbol{F}_p$, and the lines without arrows are contours of magnitude of $\boldsymbol{F}_p$.

Figure 1 shows the VMMs of a NACA0012 airfoil about different reference points, located at LE, $c/4$, $c/2$ and TE along the chordline. On the maps, a negative strength vortex provides a nose-up pitching moment if it moves so as to have a component of motion in the direction of the vortex moment lines, and the reverse is true for positive strength ones.

From the resulting VMMs, the following observations can be made:

(I) The magnitude of the VMM vectors ($|\boldsymbol{F}_p|$) decreases with the distance from the body and vanishes at infinity, which means the fact that the vorticity far away from the body should have a negligible effect on the pitching moment is satisfied automatically.

(II) The vortex moment lines point towards the reference points, which means a vortex with negative strength moving away from the reference point contributes to a nose-down pitching moment, and *vice versa*.

(III) For any reference points on the airfoil except for the LE and TE, the vortex moment lines diverge from both the LE and TE, which means a vortex with negative strength moving away from the LE/TE contributes to a nose-up pitching moment, and *vice versa*.

4. Vortex moment for viscous flows around an impulsively started NACA0012 airfoil

In this section, the VMM method is applied to an impulsively started flow around the NACA0012 airfoil. Using the velocity field provided by CFD and hence obtaining the vorticity numerically, and with the VMM vector $\boldsymbol{F}_p$ precomputed in § 3, the vortex moments are given by (2.2). Here, all of the flow field is assumed to be laminar in the CFD simulation. The theoretical moment results for pressure component M_p will be

compared to the moment obtained by the integration of the body surface pressure in the CFD code. The skin friction moment results obtained from the CFD code will also be presented to show its negligible effect. Here, the moment results will be represented in the form of non-dimensional coefficients defined as

$$C_M = \frac{M}{\frac{1}{2}\rho V_\infty^2 \zeta^2}. \tag{4.1}$$

For the NACA0012 airfoil used here, the characteristic length $\zeta = c$. The time-dependent moment will be displayed as a function of the non-dimensional time $\tau = tV_\infty/c$.

In the CFD used in this work, the Navier–Stokes (N–S) equations in unsteady laminar flow are solved numerically, with the options of a second-order upwind SIMPLE (semi-implicit method for pressure-linked equations) pressure–velocity coupling method. The flow is impulsively started at a constant speed from an initially uniform flow. Note that laminar N–S solver is adopted for all of the Reynolds numbers considered here, including the high Reynolds numbers (e.g. $Re = 1 \times 10^6$), where a laminar solver is used purely for the purpose of numerical comparison. The computational domain is $31 \times c$ in the horizontal direction and $20 \times c$ in the vertical direction. Three different mesh sizes (101 845, 180 470 and 253 300 in total; 205, 430 and 550 on the body surface) are chosen for three different Reynolds numbers (50, 1000 and 1×10^6). A minimum of 30 layers in the laminar boundary are used so that there is enough resolution in the grid size normal to the wall and in the boundary layer.

In order to validate the numerical method used here, selected numerical results for time-averaged moment for NACA 0012 and NACA 0015 airfoils at a series of AoAs from 0° up to 60° and for $Re = 1\text{–}8 \times 10^4$ are compared with those from experiments (Ohtake *et al.* 2007; Rainbird 2016) in figure 2. It is shown that the CFD results for the NACA0012 airfoil at $\alpha < 20°$ compare well with data from Ohtake *et al.* (2007). The CFD results and experimental results (Rainbird 2016) for NACA0015 at $\alpha > 20°$ are also in good agreement. Moreover, the time-averaged moments for the NACA0012 airfoil at $\alpha > 20°$ given by CFD are slightly larger than those from experiments for the NACA0015 airfoil.

In order to validate the numerical method used here, numerical results for the time-averaged moment for NACA airfoils at $Re = 1\text{–}8 \times 10^4$ are compared with those from experiments. The experimental data are collected from Ohtake *et al.* (2007) for $0° < \alpha < 20°$ and Rainbird (2016) for $20° < \alpha < 60°$. The former uses the NACA0012 airfoil while the latter uses the NACA0015 airfoil. We could not find the experimental data for the NACA0012 airfoil with $\alpha > 20°$ at such low Reynolds numbers, thus experimental data for the NACA0015 airfoil are used instead for the region of $\alpha > 20°$ since both airfoils have similar aerodynamic characteristics. Good agreement between numerical and experimental results are observed in figure 2. We would like to point out that the time-averaged moments for the NACA0012 airfoil given by CFD are slightly larger than those for the NACA0015 airfoil (from both CFD and experiments) as shown in figure 2 (i.e. when $\alpha > 20°$). This is due to the slight decrease in the thickness of the airfoil.

4.1. *Vortex moment about different reference points*

Applying the VMM method to the NACA0012 airfoil, we find good comparison between the time-dependent moment obtained by the VMM method and CFD about

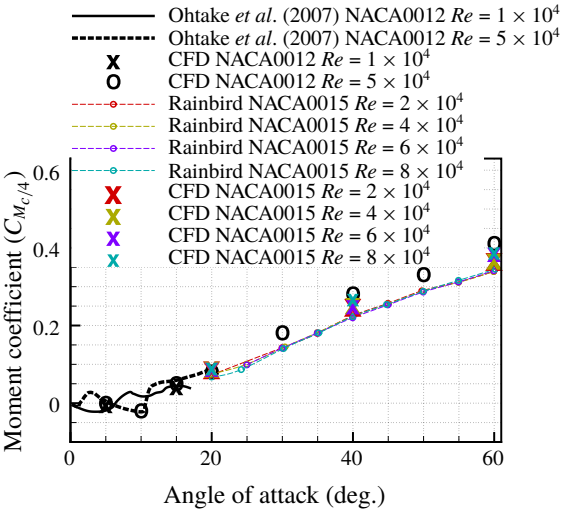

FIGURE 2. Comparison of numerical results for time-averaged moments of NACA airfoils at different angles of attack with Ohtake *et al.*'s (2007) experimental data for NACA0012 at $0° < \alpha < 20°$, and with Rainbird's (2016) experimental results for the NACA0015 airfoil at $20° < \alpha < 60°$.

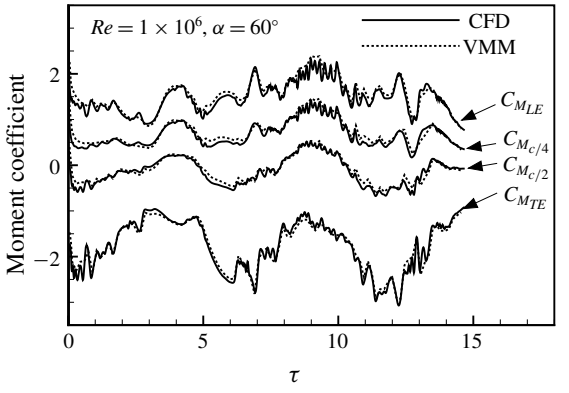

FIGURE 3. Comparison between the vortex moment method and CFD for time-dependent moment coefficients for the NACA0012 airfoil about different reference points (LE, $c/4$, $c/2$ and TE) at $Re = 1 \times 10^6$.

different reference points: LE, $c/4$, $c/2$ and TE at $Re = 1 \times 10^6$, as shown in figure 3. For the CFD results, the moment around any reference point $(x_p, 0)$ can be obtained by

$$C_{M_p} = C_{M_{c/4}} + C_L \left(x_p/c - 1/4\right) \cos\alpha + C_D(x_p/c - 1/4) \sin\alpha. \tag{4.2}$$

Here, C_L, C_D and α are the lift coefficient, the drag coefficient and the AoA, respectively. As mentioned above, there is no direct analogy between the VMM and the VFM, but according to (4.2), VMMs about different reference points are related by a superposition with the appropriate VFMs.

It is seen from figure 3 that the pitching moments at the LE and at $c/4$ are positive (nose-down) for the whole time period herein examined ($0 < \tau < 15$), while

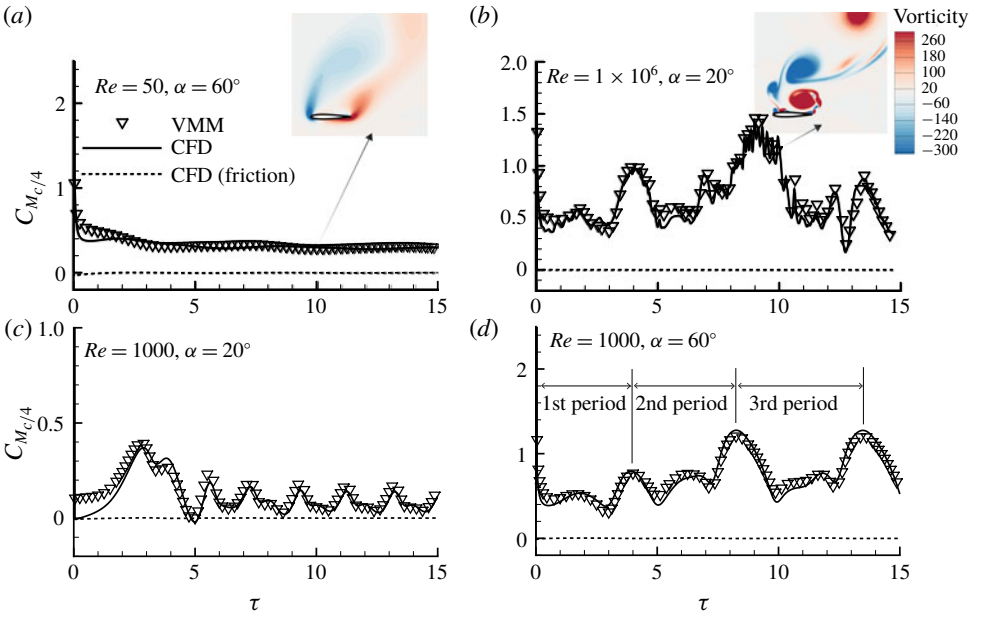

FIGURE 4. Comparison between vortex moment method and CFD for time-dependent moment coefficients for NACA0012 at different angles of attack and for different Reynolds numbers at $Re = 1 \times 10^6$.

the pitching moment at the TE is always negative (nose-up). The average value of the pitching moment at $c/4$ is higher than its steady-state value (0.39) shown in figure 2. This increment in the nose-down moment, as well as the oscillation of the unsteady pitching moment, is closely related to the alternate shedding of the LEVs and TEVs, which will be discussed in detail in § 4.3.

4.2. *Vortex moment at different AoAs and for different Reynolds numbers*

Figure 4 shows a good comparison between the VMM and CFD moment about $c/4$ of a NACA0012 airfoil for $\alpha = 20°$ and $\alpha = 60°$ at different Reynolds numbers ($Re = 50$, 1000 and 1×10^6). The friction-induced moments are shown to be very small for all Reynolds numbers presented here.

Figure 4(*a*,*b*) shows the effect of Reynolds number on the pitching moment. For a low Reynolds number ($Re = 50$), a positive (nose-down) moment decreases from infinity to a relative stable value (0.5). For a large Reynolds number ($Re = 1 \times 10^6$), after the initial drop, the moment oscillates substantially with non-dimensional time and its average value is significantly larger than 0.5. This is because the LEV and TEV in a low Reynolds number case (see figure 4*a* for the vorticity distribution) are much weaker than those in a high Reynolds number case (see figure 4*b*) and, are constrained to relatively fixed regions above the airfoil.

The time-dependent pitching moments show a clear periodicity for $Re = 1000$ due to vortex shedding (see figure 4*c*,*d*). For this specific Reynolds number, with increasing AoA, the average value and the oscillating amplitude of the moment increase while the oscillating frequency deceases. This is consistent with the well-known result that the Strouhal number decreases as the AoA increases due to the wake becoming

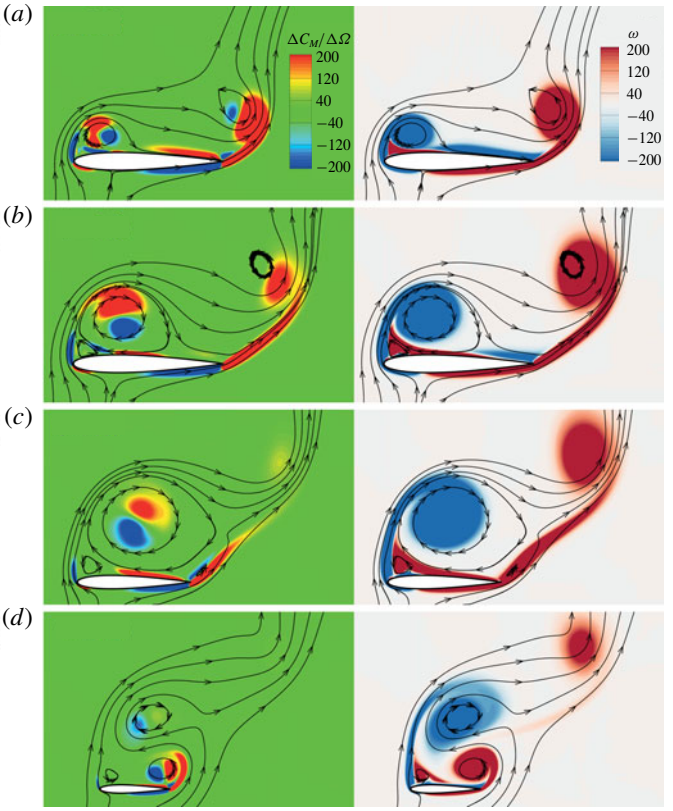

FIGURE 5. Contours of the vortex moment coefficient per unit area (left) and the vorticity (right) at typical instants: (*a*) $\tau = 0.5$, (*b*) $\tau = 1.0$, (*c*) $\tau = 2.0$, (*d*) $\tau = 3.5$, with streamlines drawn.

wider. In general, the AoA has a substantial impact on the pitching moment through changing the vortex shedding pattern, which will be further explored in the next subsection.

4.3. *Moment contribution related to the vortex evolution*

To illustrate how a quantitative understanding of the moment contribution and the evolution of the vortical field can be gained from a VMM, the moment distribution about the quarter chord is plotted in figure 5(left-hand column) for three typical instants ($\tau = 0.5$, 1, 2 and 3.5) in the first period of the starting flow of the NACA0012 airfoil at $\alpha = 60°$ and $Re = 1000$, together with contour plots of the vorticity (right-hand column). The streamlines are also shown in this figure. The vorticity contours apparently show that the vorticity is concentrated in the boundary layer vortex sheet as well as the LEVs and TEVs being shed from the body. The boundary layer vortex sheet in the rear part of the airfoil ($x/c > 1/4$) contributes significantly to the body moment, which can be attributed to the suction effect of the vortex sheet producing a positive (nose-down) pitching moment on the upper surface and a negative (nose-up) moment on the lower surface. For most snapshot instants, these positive and negative moments offset each other. It is clear that both LEVs

and TEVs consist of a positive moment contributing area (red) and a negative one (blue). As the LEV grows and convects away from the body surface, the positive area reduces and the negative area increases, resulting in a reduction on the net moment contribution. This is likely due to the concentrated LEV (with a negative strength) moving away from the LE, which has been shown to contribute a nose-up moment in figure 1. Conversely, the TEV always contributes a net nose-down moment and it can be seen that the positive contributing area is always far more significant than the negative area.

It can thus be concluded that, in the case of starting flow on a NACA0012 airfoil presented here, the increase of the moment is determined by the roll up of the TEV, whereas the decrease is caused by the LEV and TEV moving away from the body.

5. Conclusion

The VMM method for viscous flow around an arbitrary two-dimensional body has been generalized. The proposed VMM approach expresses the vortex moment as a function of the vector product of a VMM vector and the local velocity. The VMM vector can be easily obtained by solving a Laplace equation by a vortex panel method. The VMM vector, a function of the position, is independent of the flow and only dependent on the geometry of the body. Thus a VMM can be designed and precomputed to help analyse the moment contribution effect of each given vortex and, extract the moment from a flow field given by CFD or experimental data.

VMM analysis based on NACA0012 airfoil shows that a LEV moving away from the reference point or a TEV moving towards the reference point contributes to a nose-down pitching moment, and *vice versa*. Moreover, for any reference points located on the airfoil except for the LE and TE, a LEV moving away from the edges or a TEV moving towards the edges contributes to a nose-up pitching moment, and *vice versa*.

The proposed VMM method is insensitive to vortices far away from the body, and reflects the fact that pressure loads on the airfoil are mainly due to near-body vortices, in accordance with the Biot–Savart law. As a test case, the precomputed VMM, together with the vortices obtained by CFD, has been used to predict the vortex moment on an impulsively started NACA0012 airfoil. The moments given by CFD itself are used as validations. The time-averaged moments about the quarter chord of the airfoil for a range of AoAs have been compared with experimental results given by Ohtake *et al.* (2007) and Rainbird (2016). CFD has shown, as expected, that the contribution from viscous forces to the pitching moment is negligible for a large range of Reynolds numbers ($Re \geqslant 50$), which means the compact vortex moment expression derived here for inviscid flows is eligible to deal with viscous flow problems and the corresponding VMM can accurately reflect the total force contribution of the vortices in the viscous flow field. It has been found that the unsteady nose-down moment about the quarter chord is higher than the steady-state value. The increment is mainly contributed by the roll up of LEVs and TEVs. By identifying the moment contributions from LEVs and TEVs in starting flows around a NACA0012 airfoil, we have shown that a moment map could lead to an intuitive understanding of how each part of the vorticity field contributes to the pitching moment on the body. It has been found that both LEVs and TEVs consist of a positive moment contributing area and a negative one. As a LEV grows and moves away from the body, its net contribution of moment changes from positive to negative, while a TEV always contributes a net positive moment. The time variation of the total moment is the overall effect of both LEVs and TEVs.

Acknowledgements

This project has received funding from the European Union's Horizon 2020 research and innovation programme under the Marie Sklodowska-Curie grant agreement no. 765579.

Declaration of interests

The authors report no conflict of interest.

REFERENCES

BATCHELOR, G. K. 1967 *An Introduction to Fluid Dynamics*. Cambridge University Press.

CHIEREGHIN, N., CLEAVER, D. J. & GURSUL, I. 2019 Unsteady lift and moment of a periodically plunging airfoil. *AIAA J.* **57** (1), 208–222.

DEVORIA, A. C., CARR, Z. R. & RINGUETTE, M. J. 2014 On calculating forces from the flow field with application to experimental volume data. *J. Fluid Mech.* **749**, 297–319.

DICKINSON, M. H. & GOTZ, K. G. 1993 Unsteady aerodynamic performance of model wings at low Reynolds numbers. *J. Expl. Biol.* **174**, 45–64.

ELDREDGE, J. D. & JONES, A. R. Leading-edge vortices: mechanics and modeling. *Annu. Rev. Fluid Mech.* **51**, 75–104.

ELLINGTON, C. P., VAN DEN BERG, C., WILLMOTT, A. P. & THOMAS, A. L. R. 1996 Leading-edge vortices in insect flight. *Nature* **384**, 626–630.

FERNANDEZ-FERIA, R. & ALAMINOS-QUESADA, J. 2018 Unsteady thrust, lift and moment of a two-dimensional flapping thin airfoil in the presence of leading-edge vortices: a first approximation from linear potential theory. *J. Fluid Mech.* **851**, 344–373.

GRAHAM, W. R., PITT FORD, C. W. & BABINSKY, H. 2017 An impulse-based approach to estimating forces in unsteady flow. *J. Fluid Mech.* **815**, 60–76.

HAM, N. D. & MAURICE, I. Y. 1966 Torsional oscillation of helicopter blades due to stall. *J. Aircraft* **3.3**, 218–224.

HANSEN, M. H. 2007 Aeroelastic instability problems for wind turbines. *Wind Energy: Intl J. Prog. Appl. Wind Power Conversion Technol.* **10.6**, 551–577.

HOWE, M. S. 1995 On the force and moment on a body in an incompressible fluid, with application to rigid bodies and bubbles at high Reynolds numbers. *Q. J. Mech. Appl. Maths* **48**, 401–425.

KATZ, J. & PLOTKIN, A. 2001 *Low-speed Aerodynamics*, 2nd edn. Cambridge University Press.

KOUMOUTSAKOS, P., LEONARD, A. & PEPIN, F. 1994 Boundary conditions for viscous vortex methods. *J. Comput. Phys.* **113**, 52–61.

KRASHANITSA, R. Y., SILIN, D., SHKARAYEV, S. V. & ABATE, G. 2009 Flight dynamics of a flapping-wing air vehicle. *Intl J. Micro Air Vehicles* **1.1**, 35–49.

LI, J. & WU, Z. N. 2015 Unsteady lift for the Wagner problem in the presence of additional leading/trailing edge vortices. *J. Fluid Mech.* **769**, 182–217.

LI, J. & WU, Z. N. 2016 A vortex force study for a flat plate at high angle of attack. *J. Fluid Mech.* **801**, 222–249.

LI, J. & WU, Z. N. 2018 Vortex force map method for viscous flows of general airfoils. *J. Fluid Mech.* **836**, 145–166.

LIN, J. C. & ROCKWELL, D. 1996 Force identification by vorticity fields: techniques based on flow imaging. *J. Fluids Struct.* **10**, 663–668.

MANCINI, P., MANAR, F., GRANLUND, K., OL, M. V. & JONES, A. R. 2015 Unsteady aerodynamic characteristics of a translating rigid wing at low Reynolds number. *Phys. Fluids* **27** (12), 123102.

NOCA, F. (1996) On the evaluation of instantaneous fluid-dynamic forces on a bluff body. GALCIT Report FM96-5.

NOCA, F., SHIELS, D. & JEON, D. 1997 Measuring instantaneous fluid dynamic forces on bodies, using only velocity fields and their derivatives. *J. Fluids Struct.* **11**, 345–350.

OHTAKE, T., NAKAE, Y. & MOTOHASHI, T. 2007 Nonlinearity of the aerodynamic characteristics of NACA0012 aerofoil at low Reynolds numbers. *J. Japan Soc. Aeronaut. Space Sci.* **55**, 439–445.

PITT FORD, C. W. & BABINSKY, H. 2013 Lift and the leading-edge vortex. *J. Fluid Mech.* **720**, 280–313.

POLHAMUS, E. C. 1966 A concept of the vortex lift of sharp-edge delta wings based on a leading-edge-suction analogy. *NACA Technical Note*, D–3767.

RAMESH, K., GOPALARATHNAM, A., GRANLUND, K., OL, M. V. & EDWARDS, J. R. 2014 Discrete-vortex method with novel shedding criterion for unsteady aerofoil flows with intermittent leading-edge vortex shedding. *J. Fluid Mech.* **751**, 500–538.

RAINBIRD, J. M. 2016 Blockage tolerant wind tunnel testing of aerofoils at angles of incidence from 0° to 360°, with respect to the self-start of vertical-axis wind turbines. PhD thesis, Imperial College London.

WU, J. C. 1981 Theory for aerodynamic force and moment in viscous flows. *AIAA J.* **19**, 432–441.

WU, J. Z., LU, X. Y. & ZHUANG, L. X. 2007 Integral force acting on a body due to local flow structures. *J. Fluid Mech.* **576**, 265–286.

XIA, X. & MOHSENI, K. 2017 Unsteady aerodynamics and vortex-sheet formation of a two-dimensional airfoil. *J. Fluid Mech.* **830**, 439–478.

ZHAO, X., GOUDER, K., GRAHAM, J. M. R. & LIMEBEER, D. J. N. 2016 Buffet response and control of a suspension bridge section in a turbulent wind. *J. Fluids Struct.* **62**, 384–412.

ZHU, G., BEARMAN, P. W. & GRAHAM, J. M. R. 2002 Prediction of drag and lift by using velocity and vorticity fields. *Aeronaut. J.* **106** (1064), 547–554.